

# End-to-end Segmentation with Recurrent Attention Neural Network

Qiaoying Huang, Xiao Chen, Mariappan Nadar

Siemens Healthineers, Digital Technology and Innovation, Princeton, NJ, USA

{first.last, xiao-chen}@siemens-healthineers.com

## Abstract

Image segmentation quality depends heavily on the quality of the image. For many medical imaging modalities, image reconstruction is required to convert acquired raw data to images before any analysis. However, imperfect reconstruction with artifacts and loss of information is almost inevitable, which compromises the final performance of segmentation. In this study, we present a novel end-to-end deep learning framework that performs magnetic resonance brain image segmentation directly from the raw data. The end-to-end framework consists a unique task-driven attention module that recurrently utilizes intermediate segmentation result to facilitate image-domain feature extraction from the raw data for segmentation, thus closely bridging the reconstruction and the segmentation tasks. In addition, we introduce a novel workflow to generate labeled training data for segmentation by exploiting imaging modality simulators and digital phantoms. Extensive experiment results show that the proposed method outperforms the state-of-the-art methods.

## 1. Introduction

Conventionally, image segmentation tasks start from existing images. While this might seem self-evident for natural image applications, many medical imaging modalities do not acquire data in the image space. Magnetic Resonance Imaging (MRI), for example, acquires data in the spatial-frequency domain, the so-called k-space domain and the MR images needs to be reconstructed from the k-space data before further analysis. The traditional pipeline of image segmentation treats reconstruction and segmentation as separate tasks and the segmentation quality depends heavily on the quality of the image. On the other hand, under-sampling in the k-space domain, in which less data is acquired according to Nyquist theorem, is commonly used to speed up the relatively slow MRI scans. One approach to ensure segmentation quality on under-

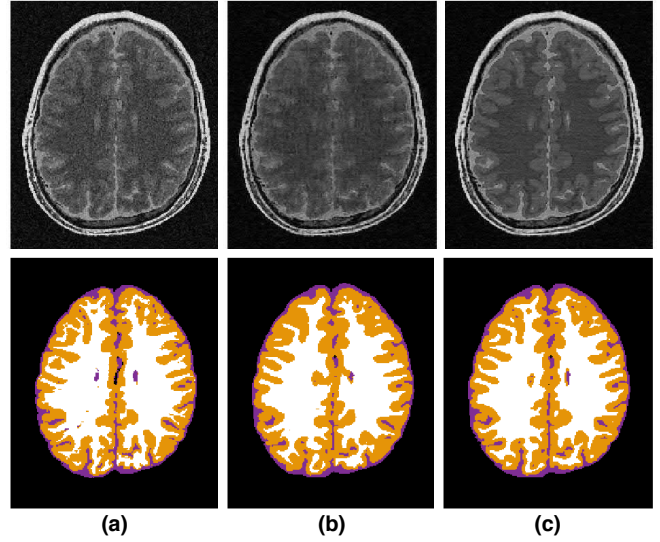


Figure 1. End-to-end brain segmentation from under-sampled k-space data. (a) The reconstructed image that is converted from fully-sampled k-space data by inverse Fourier transform and the ground truth segmentation mask. When the input k-space data is noisy and ambiguous, the quality of the reconstructed image is bad. (b) A failed case by *Joint* model that simply connects reconstruction and segmentation networks. (c) A well reconstructed image and a precise segmentation mask that are generated by our proposed model *SERANet* from noisy k-space data.

sampled MR data is to use fast imaging techniques such as parallel imaging [21, 11], partial Fourier [20] and compressed sensing (CS) [9, 5] to reconstruct images with comparable quality to the fully-sampled data.

Among these techniques, CS has been shown powerful in recovering images from highly under-sampled data, comparing to conventional fast imaging techniques. CS algorithms follow an iterative scheme to recover image contents, balancing between data measurement fidelity and image prior knowledge [18, 19]. Issues of CS reconstruction include prolonged reconstruction time and requirement of heuristic choice of image prior knowledge.

With the recent development in deep learning, there are emerging efforts of using deep neural networks for MR reconstruction [26, 25] to overcome the aforementioned issues of CS. Many studies are proposed to substitute components in CS algorithms with neural networks.

Nonetheless, even with advanced image reconstruction methods, residual artifacts, algorithm-generated artifacts and potential loss of information on the imperfect reconstructed images are almost inevitable. Without the final segmentation quality as a target, the reconstruction algorithm may discard image features that are critical for segmentation but less influential to image quality. On the other hand, it may spend most of the resources (e.g. reconstruction time) to recover image features that are less important to segmentation accuracy improvement.

Recently, an end-to-end deep learning approach is proposed [27] for MR brain image segmentation, where the network takes the k-space data as input and outputs directly the segmentation mask. While the effectiveness of combining the reconstruction and the segmentation tasks is demonstrated, their method concatenates the two tasks shallowly and only relies on backpropagation to improve feature extraction with segmentation error. It also depends on the availability of ground truth reconstructed images and is likely to fail in case of noisy raw data.

We present here an end-to-end architecture: Segmentation with End-to-end Recurrent Attention Network (*SERANet*) featuring a unique recurrent attention module that closely connects the reconstruction and the segmentation tasks. The intermediate segmentation is recurrently exploited as anatomical prior [8] that provides guidance to recover *segmentation-driven* features, which in turn improves segmentation performance. Our contributions include four aspects:

- We propose an end-to-end approach that performs image segmentation directly from under-sampled k-space data.
- We introduce a novel recurrent segmentation-aware attention module that guides the network to generate *segmentation-driven* image features to improve the segmentation performance.
- We introduce a novel workflow to generate under-sampled k-space data with oracle segmentation maps by exploiting a MRI simulator and digital brain phantoms.
- We extensively evaluate the effectiveness of the proposed method on a brain benchmark and the results show that our method consistently outperforms existing state-of-the-art approaches.

## 2. Related work

### 2.1. Image reconstruction

Donoho *et al.* [9] and Candès *et al.* [5] propose the theory of compressed sensing and Lustig *et al.* [18] first apply the CS theory to MR image reconstruction. In CS, random under-sampling is performed that leads to incoherent under-sampling artifacts in the acquired signal. The true signal can then be recovered from the acquired signal through an iterative reconstruction scheme that exploits certain domain sparsity property of the underlying signal as prior knowledge. The performance of a CS algorithm to a specific application largely depends on the choice of the hand-crafted image features. CS is also computationally expensive since it is an iterative reconstruction process.

More recently, deep learning has emerged as an effective technique to reconstruct MRI data, thanks to its powerful feature representation ability [26, 25, 13, 12, 29]. Sun *et al.* [26] develop a new network architecture called ADMM-Net based on the traditional ADMM framework. They show that deep neural network achieves good MR image reconstruction quality with less computation time. Similarly, Schlemper *et al.* [25] treat image reconstruction as a de-aliasing problem and propose a very deep neural network with cascading convolutional neural networks. Hyun *et al.* [13] propose a variant of UNet [22] for image reconstruction.

### 2.2. Image segmentation

With the recent development of using deep neural networks for natural image segmentation, promising results have been shown by extending the techniques to medical imaging segmentation. The Fully Convolutional Network (FCN) [17] achieves promising results in MR image segmentation. UNet [22] is more powerful since it captures multi-level information with skip connections and achieves the state-of-the-art in medical image segmentation in terms of accuracy and efficiency. Another variant is 3D UNet [7] that deals with volumetric data.

Attention module that guides the neural network to focus on sub-regions of the image has been successfully employed in semantic segmentation problem [14] and MR image segmentation [23] problem. For single-class attention map, all pixels with high activation score are selected. The selected attention map is multiplied with the original features, forcing the network to focus on a specific location to enhance the representation at that location while suppressing elsewhere. All these segmentation studies take images as input and assume clean images, which is impractical for clinical scenario.

### 2.3. End-to-end learning

Several end-to-end learning frameworks have been proposed for various applications [4, 16, 10, 27]. Caballero *et al.* [4] propose an unsupervised brain segmentation method that treats both reconstruction and segmentation simultaneously using patch-based dictionary sparsity model and Gaussian mixture model. Lohit *et al.* [16] extract distinctive non-linear features from CS measurements using convolutional neural networks (CNN) which is then used for image recognition. Fan *et al.* [10] propose a novel approach to guide the reconstruction task using the information from segmentation task with a multi-layer feature aggregation strategy. One work that is relevant to our work is [27] where the authors propose a unified deep neural network architecture termed *SegNetMRI* that solves reconstruction and segmentation problems simultaneously. Specifically, the reconstruction and the segmentation sub-networks are pre-trained and fine-tuned with shared reconstruction encoders. The final segmentation depends on the combination of the cascading segmentation results. The segmentation sub-network in *SegNetMRI* is trained on the reconstructed image from the original raw data, which contains artifacts and may influence the performance of segmentation.

## 3. Methods

The proposed end-to-end segmentation framework *SERANet* consists of four functional modules: reconstruction module, segmentation module, attention module and recurrent module, as shown in Figure 2. The whole model takes under-sampled k-space data as input and outputs segmentation masks. This section is arranged as follows. We start with a brief introduction to the image reconstruction module as shown in Figure 2 (a). Then we describe our general recurrent attention components that bridge the gap between reconstruction and segmentation networks to improve segmentation quality, as shown in Figure 2 (b)-(d).

### 3.1. Reconstruction from raw data

We adapt our image reconstruction using deep neural network from CS-based reconstruction algorithm. The general CS problem can be formalized as:

$$x^* = \arg \min_x \left\{ \frac{1}{2} \|F_u(x) - y\|_2^2 + \mathcal{R}(x) \right\}, \quad (1)$$

where  $x$  is estimated image and  $y$  is under-sampled k-space data.  $F_u$  is a function that performs Fourier transform followed by under-sampling. The first term in the objective function is used for data consistency that compares the regularized estimation to the actual

acquired data to ensure data fidelity. The second term  $\mathcal{R}(x)$  is a regularization term that depends on prior knowledge of data. To introduce deep neural networks into the iterative CS reconstruction framework, we use neural network blocks in place of the data consistency and the regularization term. Specifically, as shown in Figure 2 (a), the reconstruction module consists of two basic components. One component is a Data Consistency (*DC*) layer that compensates the difference in the input image and the measured k-space data. This can be formalized as the following equation:

$$x_{dc} = F^{-1}(y + \bar{\mathbf{m}} \odot F(x)), \quad (2)$$

where  $x$  is the input image,  $x_{dc}$  is the output of the *DC* layer,  $F$  is the Fourier transform and  $\mathbf{m} = \{0, 1\} \in \mathbb{R}^{1 \times w \times h}$  is the under-sampled mask indicating the position of sampling.  $\bar{\mathbf{m}}$  is the binary complement of  $\mathbf{m}$  and  $\odot$  denotes element-wise multiplication. The other component is a regularization block (*Reg* block) that takes as input the zero-filled fast Fourier transform reconstructed image  $x_0 \in \mathbb{R}^{2 \times w \times h}$  (real and imaginary parts concatenated in the first dimension), or the output from the *DC* layer  $x_{dc} \in \mathbb{R}^{2 \times w \times h}$ , and outputs an image  $x \in \mathbb{R}^{2 \times w \times h}$ . The iterative reconstruction behavior of CS reconstruction is unfolded as a series of *Den* blocks and *DC* layers. We implement two types of the *Reg* blocks: cascaded CNN (*Type A*) [25] and auto-encoder (*Type B*) [27], as two popular choices for image reconstruction using deep learning. It is worth pointing out that the reconstruction module in our method does not see any ground truth reconstruction image during the training. The recovered image content is guided by the segmentation error solely. Thus the aim of the reconstruction module is not to reconstruct the images but to recover features in the image space from the raw data that best suits the segmentation task. The usage of “reconstruction” to name the module is just for conceptual simplicity.

### 3.2. Segmentation with attention

Because the image reconstruction module is trained together with the segmentation module under our proposed end-to-end framework, it becomes possible to share useful information between reconstruction and segmentation.

One straightforward way to implement the unified training is to sequentially connect the image reconstruction module and the segmentation module. This approach is referred to as *Joint* model and can be illustrated as the combination of Figure 2 (a) and (b). The connection of two modules in this manner is shallow and only relies on backpropagation to improve reconstruction with segmentation error.

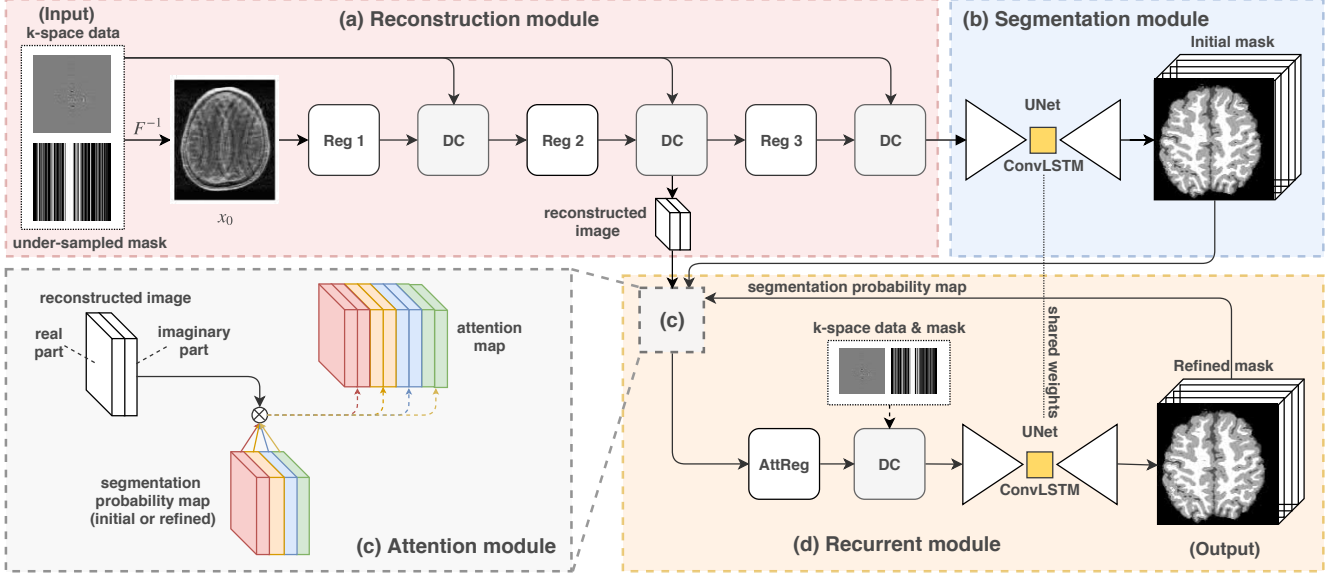


Figure 2. Illustration of the proposed end-to-end segmentation framework *SERANet*. The whole model takes the under-sampled k-space data as input and outputs segmentation masks. (a) is the reconstruction module. It takes the under-sampled k-space data as input and outputs image with decreased level of noise and artifacts. (b) is the segmentation module that takes the image learned from module (a) as input and outputs the initial segmentation mask. UNet is adopted for segmentation here. (c) is the segmentation-aware attention module to generate segmentation-driven features. (d) is the recurrent module and recurrently outputs the refined segmentation mask.

Inspired by the work [8] that utilizes segmentation mask as anatomical prior for unsupervised brain segmentation, we consider using segmentation mask to guide the image reconstruction such that the segmentation information is explicitly utilized to extract segmentation-aware image features from the raw k-space data. We adopt the attention network to facilitate the segmentation-aware learning here. Different from the traditional attention mechanism that only considers two classes in one forward pass, we propose to generate multiple-class attention maps simultaneously to distinguish features among four classes in the human brain: cerebrospinal fluid (CSF), White Matter (WM), Gray Matter (GM) and background. After one forward pass through the image reconstruction module and the segmentation module, an initial segmentation result is obtained (see Figure 2 part (b)). The segmentation maps  $s \in \mathbb{R}^{4 \times w \times h}$  have four tissue masks in separate channels, which are concatenated along the first dimension:

$$s = s^1 \oplus s^2 \oplus s^3 \oplus s^4, \quad (3)$$

where  $s^i$  indicates the  $i^{th}$  class prediction,  $\oplus$  represents concatenating along the first dimension. The segmentation mask itself is already a probability map. After a softmax layer  $\sigma(\cdot)$  that ensures the sum of the four different classes to be 1, the masks can be utilized directly for attention. Each of the four segmentation

probability maps are multiplied element-wise with the input image  $x \in \mathbb{R}^{2 \times w \times h}$  to generate new image features  $\hat{x} \in \mathbb{R}^{8 \times w \times h}$

$$\hat{x}_t = (s_t^1 \odot x_t) \oplus (s_t^2 \odot x_t) \oplus (s_t^3 \odot x_t) \oplus (s_t^4 \odot x_t), \quad (4)$$

as shown in Figure 2 (c) the Attention module. Subscription  $t$  represents the  $t^{th}$  intermediate result. The new image features  $\hat{x}_t$  go through an image feature extraction module that consists of one *Reg* block for attention features (referred as *AttReg*) and one *DC* layer. The difference between *AttReg* and *Reg* in the reconstruction module is the input channel size of *AttReg* is 8 instead of 2. The output of the attention-assisted image feature extraction is then fed to the same segmentation module with shared weights to generate a new segmentation estimation  $s_{t+1}$ . Formally,  $s_{t+1}$  can be expressed as follows.

$$s_{t+1} = (f_{\text{Segmentation}} \circ f_{\text{DC}} \circ f_{\text{AttReg}})(\hat{x}_t), \quad (5)$$

where  $s_{t+1}$  is the new segmentation estimation. By explicitly utilizing intermediate segmentation results for reconstruction, or more precisely image feature extraction, segmentation-driven features will be generated, which in turn improves segmentation performance during training with back-propagation algorithm. It can be seen from Figure 1 (c) that clear boundaries are generated using the proposed *SERANet* from under-



sampled k-space data, while the ground truth reconstruction from fully-sampled k-space data contains noise. UNet is adopted in this study for the segmentation module. It is worth pointing out that the proposed framework is not limited to a specific network model for the segmentation task.

### 3.3. Recurrent attention network

In the proposed framework, the segmentation-aware reconstruction and the segmentation is performed recurrently, as illustrated in Figure 2 (d). The recurrent procedure is described as follows. At  $t^{th}$  recurrence, segmentation is first performed on image  $x_t$  to obtain tissue mask  $s_t$  according to equation 3. Mask  $s_t$  is considered as attention map to generate new attention-assisted image  $\hat{x}_t$  from equation 4. Then a new segmentation mask  $s_{t+1}$  is predicted based on  $\hat{x}_t$ . The following equation summarizes the recurrent module:

$$s_{t+1} = g(s_t, x_t), \quad (6)$$

where  $g$  is the composition of equation 3 to equation 5. To capture the spatial information at different recurrences, a ConvLSTM layer [28] is integrated into the UNet for segmentation.

The general objective function of the whole model is defined as  $L = \mathcal{L}_{ce}(s_T, s_{gt})$ , where  $s_{gt}$  is the ground truth segmentation maps of the four classes and  $\mathcal{L}_{ce}$  is the cross entropy loss function on segmentation results. Here,  $s_T$  denotes the output of the final iteration. We also provide all the network structures and implementation details in the supplementary material.

## 4. Experiments

We extensively evaluate the proposed method in this section. Firstly, we describe a novel workflow to generate training data with ground truth segmentation maps. Secondly, we compare the proposed method thoroughly with other approaches. Finally, we investigate how the performance of the method varies under different model settings.

### 4.1. Data generation

One challenge for end-to-end segmentation learning is the preparation of the raw acquisition data and the corresponding ground truth segmentation. Most current studies simulate the raw k-space data from real-valued DICOM images. However, MR by nature is complex-valued and the k-space data from the Fourier transformed image is oversimplified with unrealistic Hermitian symmetry. Even if complex-valued images are used, the originally acquired k-space can rarely be recovered from the images alone due to common MR

post-processing practices such as multi-coil acquisition, bias field correction and etc. The simulated k-space from images is far from real acquisition. It is also hard to obtain the ground truth segmentation for training. Manual labeling is commonly used, but it is time and labor consuming and prone to error for small anatomy structures. What’s more critical here is that manual labeling is performed on images. It is thus required to choose a specific reconstruction algorithm to reconstruct images from the raw data and the specific algorithm may provide noisy, distorted images and biased algorithm-related features. This practice contradicts with the motivation of using an end-to-end training framework.

We propose here a novel method to generate realistic k-space data with ground truth segmentation mask. Specifically, a widely utilized MRI scanner simulator MRiLab [15, 2] is adopted to provide a realistic virtual MR scanning environment, which includes scanner system imperfection, MR acquisition pattern and MR data generation and recording. We use publicly available digital brain phantoms from BrainWeb [6, 1] as the object “scanned” in the MRI simulator. Each digital brain is a 3D volume of MR physics parameters such as T1, T2, which are not images per se. These parameters are then used in the simulator for MR signal generation through MR physics simulation. The BrainWeb dataset contains *20 Anatomical Models of Normal Brains* where each brain consists of 11 tissue types with the spatial distributions of each tissue. The availability of these ground truth segmentation maps avoids manual segmentation error, especially at tissue boundaries where accurate segmentation is challenging due to partial volume effect. We setup the digital brain by using clinical recommended T1, T2 and T2\* values for each tissue according to [3]. All 20 digital brains are downsampled and cropped to have a unified size of  $180 \times 216 \times 180$  with 1 mm isotropic resolution. Fully-sampled k-space data is then simulated by scanning the digital brains in MRiLab. A spin echo sequence with Cartesian readout is used with average TE = 80 ms and average TR = 3 s. 5% variation of both TE and TR values are used for the scanning. Multiple 2D axial slices are scanned for each 3D volume with slice thickness = 3 mm. Total  $57 \times 20 = 1140$  2D slices are generated. 969 slices of 17 brains are used for training and the rest 171 slices from 3 brains are reserved for testing only. Each slice has the corresponding tissue segmentation mask from BrainWeb. Three main tissue types: CSF, GM and WM are the targeted segmentation classes, and the rest 8 tissues are grouped together with air background as the background class. We use a zero-mean Gaussian distribution with a densely sampled k-space

Table 1. Segmentation results of compared methods on 171 test data with under-sampled rate of 70% (30% of fully-sampled data). Mean Dice and Hausdorff distance are reported for CSF, Gray Matter, White Matter tissues and average performance. Results from reconstruction models using cascaded CNN (*Type A*) and UNet (*Type B*) are both presented.

Methods	CSF		Gray Matter		White Matter		Average	
	Dice	HD	Dice	HD	Dice	HD	Dice	HD
<i>Fully-sampled</i>	0.8928	3.9399	0.9512	3.7535	0.9344	3.4630	0.9261	3.7188
<i>Zero-filling</i>	0.7677	4.6895	0.8334	5.7635	0.7900	5.1125	0.7970	5.1885
<i>SegNetMRI</i>	0.8370	4.2503	0.8934	5.0081	0.8580	4.4876	0.8628	4.5820
Reconstruction <i>Type A</i>								
<i>Two-step</i>	0.8355	4.3036	0.8825	5.0945	0.8501	4.5963	0.8560	4.6648
<i>Joint</i>	0.8302	4.386	0.8845	4.9957	0.8552	4.5015	0.8566	4.6277
<i>SERANet-1 (ours)</i>	0.8455	4.2260	0.9039	4.8184	0.8742	4.3198	0.8745	4.4547
<i>SERANet-2 (ours)</i>	0.8445	4.2073	0.9049	4.7668	0.8752	4.3144	0.8749	4.4295
<i>SERANet-3 (ours)</i>	0.8422	<b>4.1874</b>	0.9051	4.7709	0.8774	4.3277	0.8749	4.4287
<i>SERANet-3++ (ours)</i>	<b>0.8519</b>	4.1901	<b>0.9132</b>	<b>4.6586</b>	<b>0.8865</b>	<b>4.1667</b>	<b>0.8839</b>	<b>4.3385</b>
Reconstruction <i>Type B</i>								
<i>Two-step</i>	0.8376	4.2743	0.8928	4.9838	0.8588	4.4832	0.8631	4.5804
<i>Joint</i>	0.8346	4.2396	0.8946	4.8750	0.8663	4.4226	0.8652	4.5124
<i>SERANet-1 (ours)</i>	0.8485	4.2155	0.9064	4.7270	0.8798	4.2604	0.8752	4.4010
<i>SERANet-2 (ours)</i>	0.8534	<b>4.1579</b>	0.9129	4.6539	0.8872	4.1877	0.8845	4.3332
<i>SERANet-3 (ours)</i>	0.8528	4.1955	<b>0.9130</b>	4.6490	0.8876	4.2005	0.8845	4.3483
<i>SERANet-3++ (ours)</i>	<b>0.8575</b>	4.1736	0.9124	<b>4.6150</b>	<b>0.8895</b>	<b>4.1610</b>	<b>0.8865</b>	<b>4.3165</b>

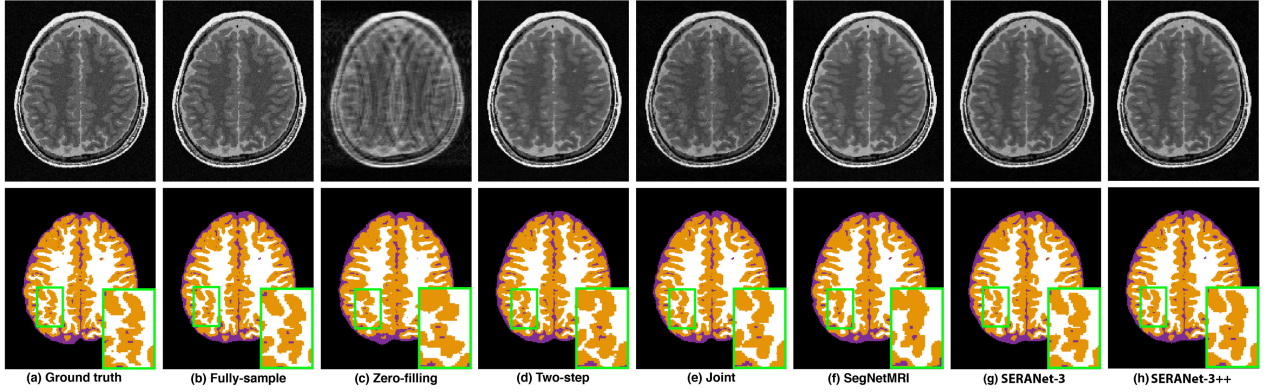


Figure 3. Segmentation performance on example image with reconstruction *Type A*. The areas where our *SERANet* models perform better than other methods are highlighted by the green bounding boxes.

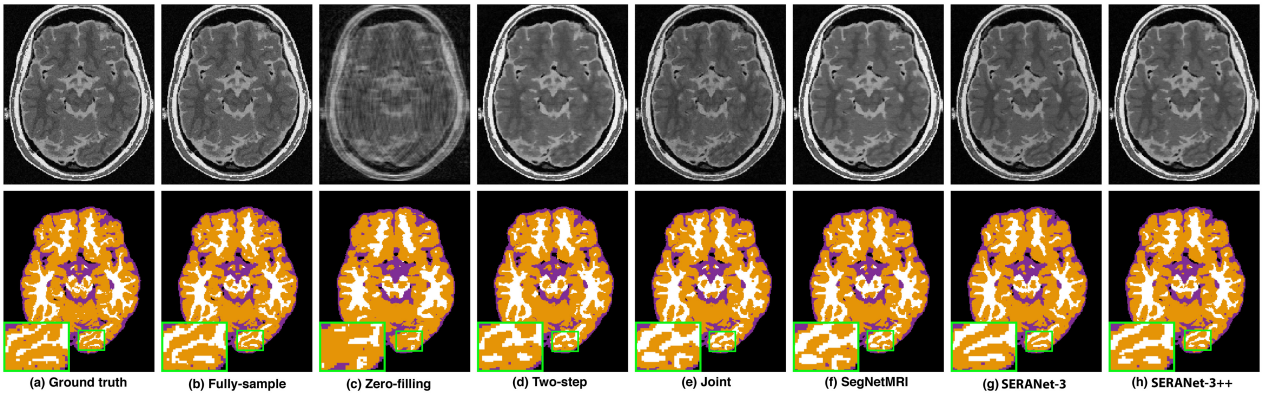


Figure 4. Segmentation performance on example image with reconstruction *Type B*. The areas where our *SERANet* models perform better than other methods are highlighted by the green bounding boxes.

center to realize a pseudo-random under-sampling pattern. For the experiment, 30% phase encoding lines are maintained with 16 center k-space lines.

## 4.2. Evaluation

To evaluate the proposed *SERANet*, we compare our method to conventional learning methods that take images as input, and to methods that take k-space as input but handle the image reconstruction and segmentation tasks differently. Specifically, the following approaches have been implemented:

- *Fully-sampled* is a segmentation model that learns to segment on fully-sampled image. The image is directly calculated using inverse Fourier transform of the fully-sampled k-space. This method is expected to provide best achievable performance.
- *Zero-filling* is a segmentation model that learns to segment directly on under-sampled image. The under-sampled k-space is zero-filled at missing k-space locations and inverse Fourier transformed to reconstruct the image. We expect this method to give the lower bound of performance.
- *Two-step* contains separate reconstruction and segmentation modules which are trained separately as well. It serves as a baseline model for segmentation tasks that start from k-space data.
- *Joint* contains separate reconstruction and segmentation modules similar as those in *Two-step*, but the two parts are trained together. This is an end-to-end model with simple concatenation of reconstruction and segmentation.
- *SegNetMRI* is the model proposed by [27]. It jointly trains a concatenated reconstruction and segmentation network with multiple shared encoders. The sub-networks are first pre-trained separately before being fine-tuned by both reconstruction loss and segmentation loss together.
- *SERANet-N* is our proposed recurrent attention model that repeats attention module  $N$  times.
- *SERANet-N++* is our proposed recurrent attention model that is initialized by pre-trained reconstruction and segmentation weights and then fine-tuned only by the segmentation loss.

For the reconstruction model and the *Reg* block in the proposed method, both cascaded CNN (*Type A* [25]) and auto-encoder (*Type B* [27]) are tested. For the segmentation model, we adopt a UNet with similar structure as *Type B* but with additional layers. All models are implemented in Pytorch and trained on NVIDIA TITAN Xp. Hyperparameters are set as: a learning rate of  $10^{-4}$  with decreasing rate of 0.5 for every 20

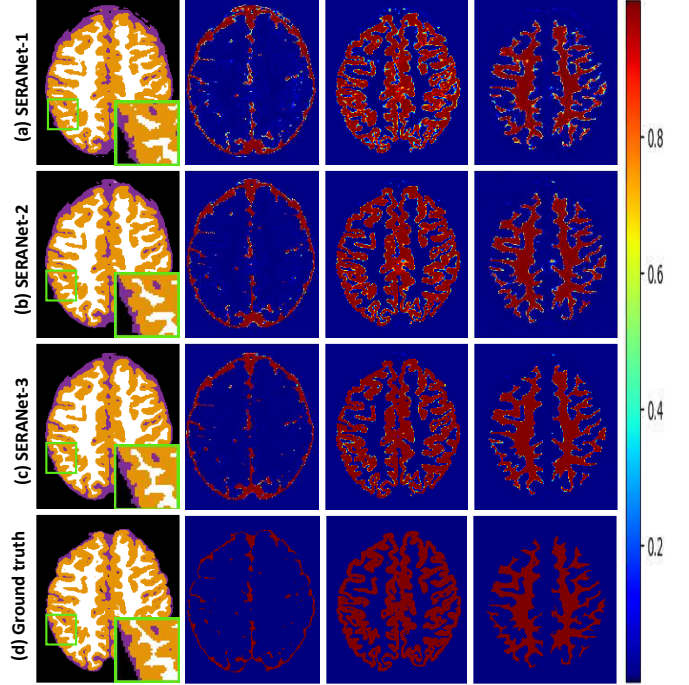


Figure 5. Intermediate attention maps of our recurrent attention model. It shows attention maps are gradually refined through increasing number of recurrence.

epochs, 50 maximum epochs, batch size of 12. Adam optimizer is used in training all the networks.

**Quantitative results** We measure the performance of all methods using Dice and Hausdorff distance (HD). Higher Dice and lower HD scores indicate better segmentation quality. As shown in Table 1, we observe following three trends. First, all proposed models that with attention *SERANet-1*, *SERANet-2*, *SERANet-3* and *SERANet-3++* outperform the *Two-step*, *Joint* and *SegNetMRI* model in terms of Dice and HD values, in all segmentation tasks regardless of the choice of reconstruction model type. In the category of using reconstruction model *Type A*, for the average performance among our proposed methods, *SERANet-3++* achieves the highest Dice score of 0.8839 and the lowest HD score of 4.3385. For all the other methods, *SegNetMRI* achieves the highest Dice score of 0.8628 and the lowest HD score of 4.5820. Our methods improve the performance of the best comparison by 0.0211 increase in Dice and 0.2435 decrease in HD. According to [24], in brain segmentation problem, the increase of performance is striking, and hence limited improvement is still promising. We observe similar results in the segmentation task of all three tissues in *Type B*. Also, note that the segmentation performance of *Type B* is slightly better than *Type A*.

Second, the segmentation quality from *SERANet-N*



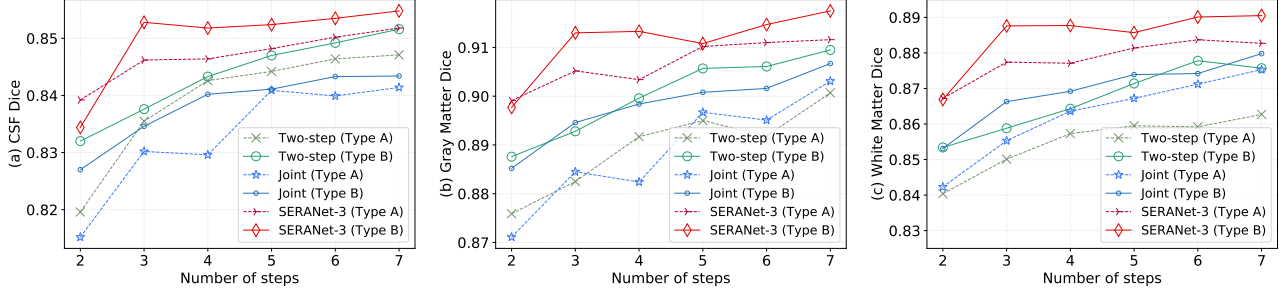


Figure 6. Dice score as a function of the number of reconstruction blocks on (a) CSF, (b) Gray Matter and (c) White Matter.

increases with increasing number of recurrent blocks in most cases. Take *Type A* as an example. The *SERANet-2* model gains better performance than the *SERANet-1* model in terms of Dice scores and HD scores. The *SERANet-3* model achieves the lowest HD score of 4.4287. We observe that in both *Type A* and *Type B* cases, the whole model has converged by repeating the recurrent module three times.

Third, the proposed model *SERANet-N++* that uses pre-trained weights is better than *SERANet-N* that does not. By conditioning the reconstruction module using the reconstruction ground truth as a start point, the *Attention 3++* model achieves the highest Dice and the lowest HD score in all cases. Different from *SegNetMRI*, the proposed *SERANet-3++* is finetuned only by segmentation loss. This avoids using noisy “ground truth” images that may not be suitable for segmentation, which makes the whole training process completely end-to-end.

**Qualitative results** We visualize two segmentation examples using different reconstruction blocks: *Type A* (shown in Figure 3) and *Type B* (shown in Figure 4). CSF, Gray Matter and White Matter parts in each brain are colorized with purple, orange and white, respectively. The green rectangle includes an example region where the proposed methods outperform the other methods. For example, the *SERANet-3* and *SERANet-3++* have more accurate white matter segmentation result. We also display the reconstructed images in the first row of Figure 3 and Figure 4. Even if our method *SERANet-3* does not employ the reconstruction ground truth, it still generates meaningful results compared to other models that utilize ground truth reconstruction information. What’s more, the image generated by *SERANet-3* (Figure 4 (g)) has a better contrast between different tissues than the image by *Joint* model. Our network can learn better feature representation that is beneficial for segmentation which may be due to the explicit use of the attention module.

To better evaluate the effect of recurrence, we also show the probability (attention) maps of three tis-

sues at different recurrent times along with the ground truth. As shown in Figure 5, the segmentation estimation of the regions which are ambiguous (probabilities around 0.5) at the first recurrence (Figure 5 (a)) gradually becomes more distinctive through recurrence (Figure 5 (c)).

### 4.3. Effects of repeated blocks

As we discussed in the section 3.1, the cascading CNN reconstruction network works in a similar way as the iterative procedures in the CS-based method. It is expected that with more cascading reconstruction blocks, the recovered image features become better in quality and more suitable for segmentation. In Figure 6, the segmentation Dice score is plotted against number of reconstruction blocks for *Two-step*, *Joint* and the proposed *SERANet-3*. We observe that in all three tissues the Dice scores improve as the number of blocks increases. In both *Type A* and *Type B*, our proposed *SERANet-3* models outperform the *Two-step* and *Joint* models. The methods based on auto-encoder (*Type B*) are better than those based on cascading CNN (*Type A*).

## 5. Conclusions

In this paper, we propose a novel end-to-end approach *SERANet* for MR brain segmentation, which performs segmentation directly on under-sampled k-space data via a recurrent segmentation-aware attention mechanism. The attention module closely connects the reconstruction and the segmentation networks and recurrently focuses on learning attention to regions of segmentation so that both image feature extraction and segmentation performance are improved. Moreover, we design a training data generation workflow to simulate realistic MR scans on digital brain phantoms with ground truth segmentation masks. Extensive experiments are conducted and the results demonstrate the effectiveness and the superior performance of our model.



## References

- [1] Brainweb: Simulated brain database. <http://www.bic.mni.mcgill.ca/brainweb/>, 2018. Accessed 16-Nov-2018. 5
- [2] Mrilab: A numerical mri simulator. <http://mrilab.sourceforge.net/>, 2018. Accessed 16-Nov-2018. 5
- [3] B. Aubert-Broche, A. C. Evans, and L. Collins. A new improved version of the realistic digital brain phantom. *NeuroImage*, 32(1):138–145, 2006. 5
- [4] J. Caballero, W. Bai, A. N. Price, D. Rueckert, and J. V. Hajnal. Application-driven mri: Joint reconstruction and segmentation from undersampled mri data. In *International Conference on Medical Image Computing and Computer-Assisted Intervention*, pages 106–113. Springer, 2014. 3
- [5] E. J. Candès et al. Compressive sampling. In *Proceedings of the international congress of mathematicians*, volume 3, pages 1433–1452. Madrid, Spain, 2006. 1, 2
- [6] R. K.-S. K. A. C. E. Chris A. Cocosco, Vasken Kollokian. Brainweb: Online interface to a 3d mri simulated brain database, 1997. 5
- [7] Ö. Çiçek, A. Abdulkadir, S. S. Lienkamp, T. Brox, and O. Ronneberger. 3d u-net: learning dense volumetric segmentation from sparse annotation. In *International Conference on Medical Image Computing and Computer-Assisted Intervention*, pages 424–432. Springer, 2016. 2
- [8] A. V. Dalca, J. Guttag, and M. R. Sabuncu. Anatomical priors in convolutional networks for unsupervised biomedical segmentation. In *Proceedings of the IEEE Conference on Computer Vision and Pattern Recognition*, pages 9290–9299, 2018. 2, 4
- [9] D. L. Donoho. Compressed sensing. *IEEE Transactions on information theory*, 52(4):1289–1306, 2006. 1, 2
- [10] Z. Fan, L. Sun, X. Ding, Y. Huang, C. Cai, and J. Paisley. A segmentation-aware deep fusion network for compressed sensing mri. *arXiv preprint arXiv:1804.01210*, 2018. 3
- [11] M. A. Griswold, P. M. Jakob, R. M. Heidemann, M. Nittka, V. Jellus, J. Wang, B. Kiefer, and A. Haase. Generalized autocalibrating partially parallel acquisitions (grappa). *Magnetic Resonance in Medicine: An Official Journal of the International Society for Magnetic Resonance in Medicine*, 47(6):1202–1210, 2002. 1
- [12] K. Hammernik, T. Klatzer, E. Kobler, M. P. Recht, D. K. Sodickson, T. Pock, and F. Knoll. Learning a variational network for reconstruction of accelerated mri data. *Magnetic resonance in medicine*, 79(6):3055–3071, 2018. 2
- [13] C. M. Hyun, H. P. Kim, S. M. Lee, S. Lee, and J. K. Seo. Deep learning for undersampled mri reconstruction. *arXiv preprint arXiv:1709.02576*, 2017. 2
- [14] K. Li, Z. Wu, K. Peng, J. Ernst, and Y. Fu. Tell me where to look: Guided attention inference network. *CoRR*, abs/1802.10171, 2018. 2
- [15] F. Liu, J. V. Velikina, W. F. Block, R. Kijowski, and A. A. Samsonov. Fast realistic mri simulations based on generalized multi-pool exchange tissue model. *IEEE transactions on medical imaging*, 36(2):527–537, 2017. 5
- [16] S. Lohit, K. Kulkarni, and P. Turaga. Direct inference on compressive measurements using convolutional neural networks. In *Image Processing (ICIP), 2016 IEEE International Conference on*, pages 1913–1917. IEEE, 2016. 3
- [17] J. Long, E. Shelhamer, and T. Darrell. Fully convolutional networks for semantic segmentation. In *Proceedings of the IEEE Conference on Computer Vision and Pattern Recognition*, pages 3431–3440, 2015. 2
- [18] M. Lustig, D. Donoho, and J. M. Pauly. Sparse mri: The application of compressed sensing for rapid mr imaging. *Magnetic resonance in medicine*, 58(6):1182–1195, 2007. 1, 2
- [19] S. Ma, W. Yin, Y. Zhang, and A. Chakraborty. An efficient algorithm for compressed mr imaging using total variation and wavelets. In *Proceedings of the IEEE conference on Computer Vision and Pattern Recognition*, pages 1–8. IEEE, 2008. 1
- [20] D. C. Noll, D. G. Nishimura, and A. Macovski. Homodyne detection in magnetic resonance imaging. *IEEE transactions on medical imaging*, 10(2):154–163, 1991. 1
- [21] K. P. Pruessmann, M. Weiger, M. B. Scheidegger, and P. Boesiger. Sense: sensitivity encoding for fast mri. *Magnetic resonance in medicine*, 42(5):952–962, 1999. 1
- [22] O. Ronneberger, P. Fischer, and T. Brox. U-net: Convolutional networks for biomedical image segmentation. In *International Conference on Medical image computing and computer-assisted intervention*, pages 234–241. Springer, 2015. 2
- [23] A. G. Roy, N. Navab, and C. Wachinger. Concurrent spatial and channel squeeze & excitation in fully convolutional networks. *CoRR*, abs/1803.02579, 2018. 2
- [24] A. G. Roy, N. Navab, and C. Wachinger. Concurrent spatial and channel squeeze & excitation in fully convolutional networks. *arXiv preprint arXiv:1803.02579*, 2018. 7
- [25] J. Schlemper, J. Caballero, J. V. Hajnal, A. Price, and D. Rueckert. A deep cascade of convolutional neural networks for mr image reconstruction. In *International Conference on Information Processing in Medical Imaging*, pages 647–658. Springer, 2017. 2, 3, 7, 10
- [26] J. Sun, H. Li, Z. Xu, et al. Deep admm-net for compressive sensing mri. In *Advances in Neural Information Processing Systems*, pages 10–18, 2016. 2
- [27] L. Sun, Z. Fan, Y. Huang, X. Ding, and J. Paisley. Joint CS-MRI reconstruction and segmentation with a unified deep network. *CoRR*, abs/1805.02165, 2018. 2, 3, 7, 10
- [28] S. Xingjian, Z. Chen, H. Wang, D.-Y. Yeung, W.-K. Wong, and W.-c. Woo. Convolutional lstm network:

A machine learning approach for precipitation now-casting. In *Advances in neural information processing systems*, pages 802–810, 2015. 5

- [29] B. Zhu, J. Z. Liu, S. F. Cauley, B. R. Rosen, and M. S. Rosen. Image reconstruction by domain-transform manifold learning. *Nature*, 555(7697):487, 2018. 2

## Supplementary Material

In this supplementary material, we include more implementation details and experimental results.

### A. Additional Implementation Details

In this paper, we consider a segmentation problem with four brain segmentation masks: 0-Background, 1-CSF, 2-Gray Matter and 3-White Matter. As mentioned in the paper, these four masks are adapted from original 11 brain tissues. The reason to use the four masks is that CSF, Gray Matter and White Matter cover most parts of the brain, as shown in Figure 7 (a) and (b). The other eight tissues, such as vessels, skulls and skins, are grouped as Background mask.

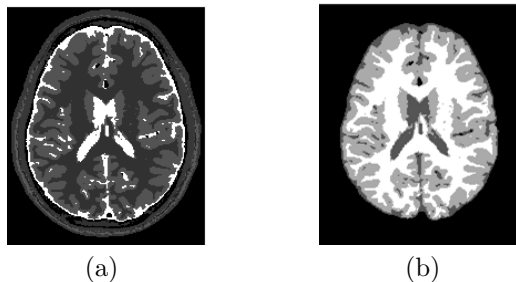


Figure 7. (a) Original 11 tissues segmentation masks. (b) Selected 4 tissues segmentation masks.

#### A.1. Data generation

The detailed data generation process is illustrated in Figure 8. Given fully-sampled k-space data (top-left), we first randomly generate under-sampled mask, e.g. with 70% sampling rate (top-middle). Under-sampled k-space data (top-right) is obtained by employing the mask on the fully-sampled k-space data. Then, fully-sampled image (bottom-left) can be generated from fully-sampled k-space data via inverse fast Fourier transform. Note that the fully-sampled image is used as ground truth by some existing algorithms, however, it may contain noise and comprise the segmentation performance. Similarly, zero-filling image (bottom-right) is generated from under-sampled k-space data via inverse Fourier transform, and is taken as the input in all models.

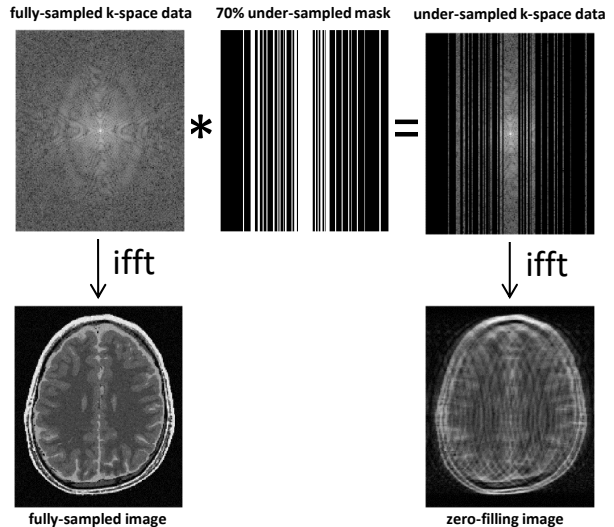


Figure 8. The process to generate under-sampled k-space data.

#### A.2. Network architectures

In our SERANet, we implement two types of regularization blocks: cascaded CNN (Type A) [25] and auto-encoder (Type B) [27], which are two popular choices for image reconstruction using deep learning. Their architectures are respectively shown in Figure 9 (a) and 9 (b). We also show the architecture of the UNet adopted in the paper for the segmentation module in Figure 9 (c).

### B. Additional Experiment on Noisy Data

In this section, we provide additional quantitative and qualitative results with an emphasis on noisy data. In our paper, we already demonstrated the results on data with 10% white Gaussian noise. Now, we generate data with 20% white Gaussian noise and show results of our SERANet and the other methods. We also include two videos named “SERANet-3-image.avi” and “SERANet-3-seg.avi” in this supplementary material package to show all the reconstructed images and segmentation masks of one subject.

#### B.1. Quantitative Results

As shown in Table 2, the proposed method SERANet achieves best result among all the tested methods. Specifically, compared with results on data with 10% white Gaussian noise, the performance of the SegNetMRI [27] is heavily affected by the noisy input data with 20% noise. The proposed SERANets are more stable and robust even at higher noise level.

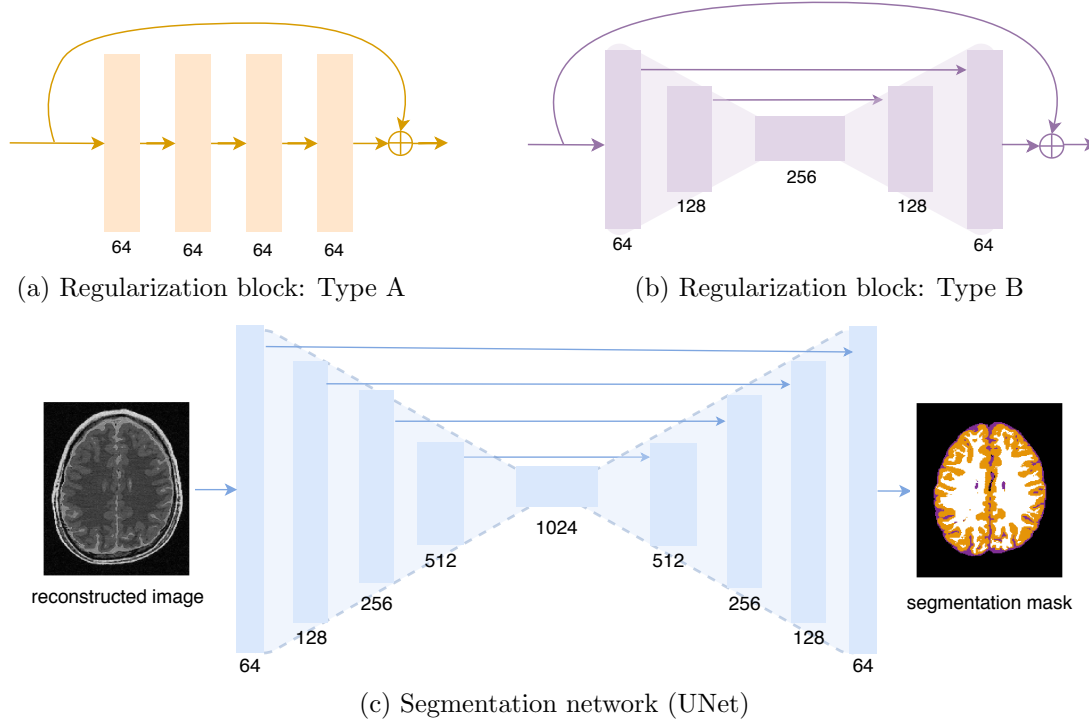


Figure 9. Achitectures of two regularization blocks and one segmentation network utilized in the paper.

Table 2. Segmentation results of all the tested methods on 171 test data with 20% white Gaussian noise and under-sampling rate of 70% (30% of fully-sampled data). Mean Dice and Hausdorff distance (HD) are reported for CSF, Gray Matter, White Matter tissues and average performance. Results from reconstruction models using cascaded CNN (Type A) and UNet (Type B) are both presented.

Methods	CSF		Gray Matter		White Matter		Average	
	Dice	HD	Dice	HD	Dice	HD	Dice	HD
Fully-sample	0.8631	4.0475	0.9188	4.4591	0.8946	4.0429	0.8922	4.1832
Zero-filling	0.7600	4.7199	0.8324	5.7391	0.7911	5.0927	0.7945	5.1839
SegNetMRI	0.7793	4.7487	0.8384	5.6724	0.7753	5.0391	0.7977	5.1534
Reconstruction Type A								
Two-step	0.7988	4.4920	0.8567	5.5001	0.8194	4.8873	0.8250	4.9598
Joint	0.7997	4.4992	0.8584	5.4482	0.8125	4.8627	0.8235	4.9367
SERANet-1	0.8079	<b>4.4971</b>	<b>0.8726</b>	5.2571	0.8409	4.6497	<b>0.8405</b>	<b>4.8013</b>
SERANet-2	0.8079	4.5132	0.8684	5.2568	0.8408	4.6745	0.8390	4.8148
SERANet-3	0.8064	4.5159	0.8684	<b>5.2408</b>	<b>0.8425</b>	4.6619	0.8391	4.8062
SERANet-3++	<b>0.8075</b>	4.5183	0.8693	5.2589	0.8421	<b>4.6358</b>	0.8396	4.8043
Reconstruction Type B								
Two-step	0.8079	4.5826	0.8654	5.5678	0.8243	5.0000	0.8325	5.0501
Joint	0.8084	4.4488	0.8694	5.3607	0.8223	4.7869	0.8334	4.8655
SERANet-1	0.8122	4.4684	0.8740	5.1799	0.8478	4.6194	0.8447	4.7559
SERANet-2	0.8108	4.4939	0.8684	5.2075	0.8408	4.6300	0.8400	4.7772
SERANet-3	0.8115	4.4763	0.8717	5.1993	0.8460	4.6188	0.8431	4.7648
SERANet-3++	<b>0.8155</b>	<b>4.4312</b>	<b>0.8756</b>	<b>5.1584</b>	<b>0.8514</b>	<b>4.5959</b>	<b>0.8475</b>	<b>4.7285</b>

## B.2. Qualitative Results

We present more examples of the reconstructed image and the segmentation mask obtained from differ-

ent methods with input of 20% white Gaussian noise in Figure 10 and 11. CSF, Gray Matter and White Matter parts in each brain are colored with purple, orange and white, respectively. The images reconstructed

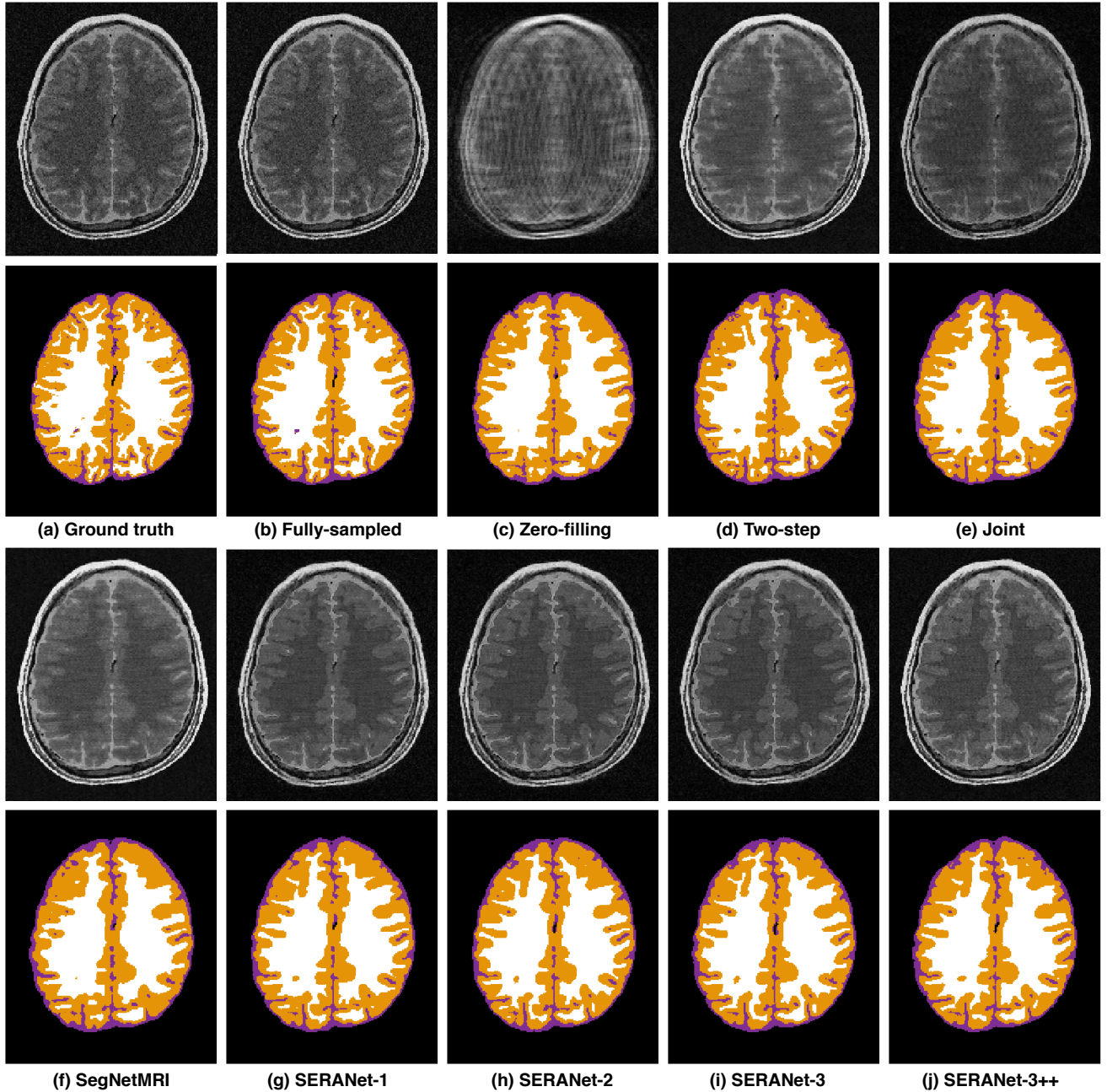


Figure 10. Segmentation performance on input data with 20% white Gaussian noise with reconstruction Type A.

by our SERANet model are barely affected by the increased noise level. The contrast between different tissues on the SERANet results are better than those from Two-step, Joint and SegNetMRI models. Our network can learn better image feature representation that is beneficial for segmentation. This can be due to the use of the attention module.

We also show the probability map of three tissues on the noisier data to better evaluate the robustness

and effectiveness of our model. As shown in Figure 12, the segmentation estimation becomes more accurate with increasing number of recurrences. Moreover, the boundaries of reconstructed images generated by our SERANet-N models become clearer than that by the Joint model and the input noisy ground truth.



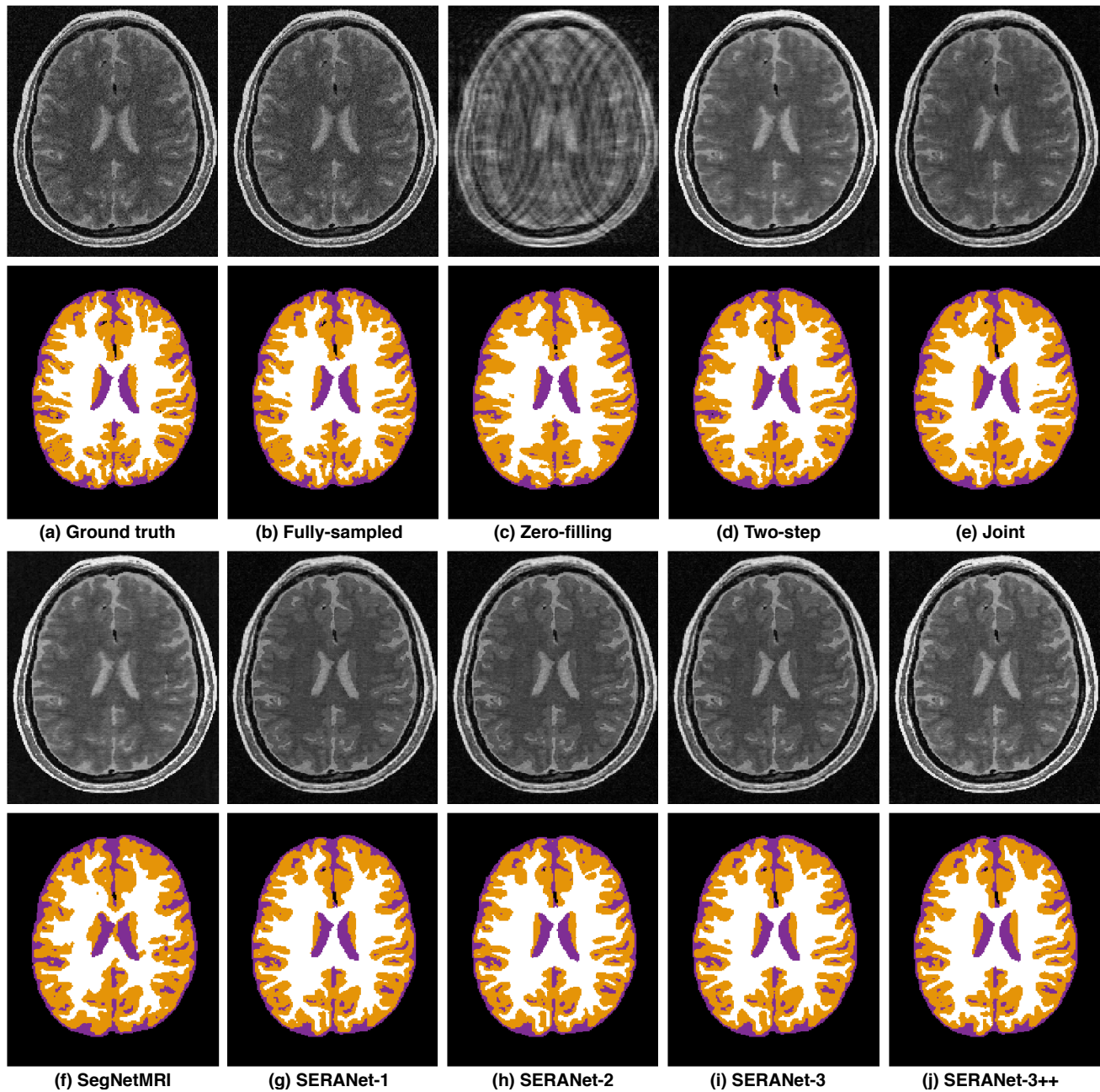


Figure 11. Segmentation performance on input data with 20% white Gaussian noise with reconstruction Type B.

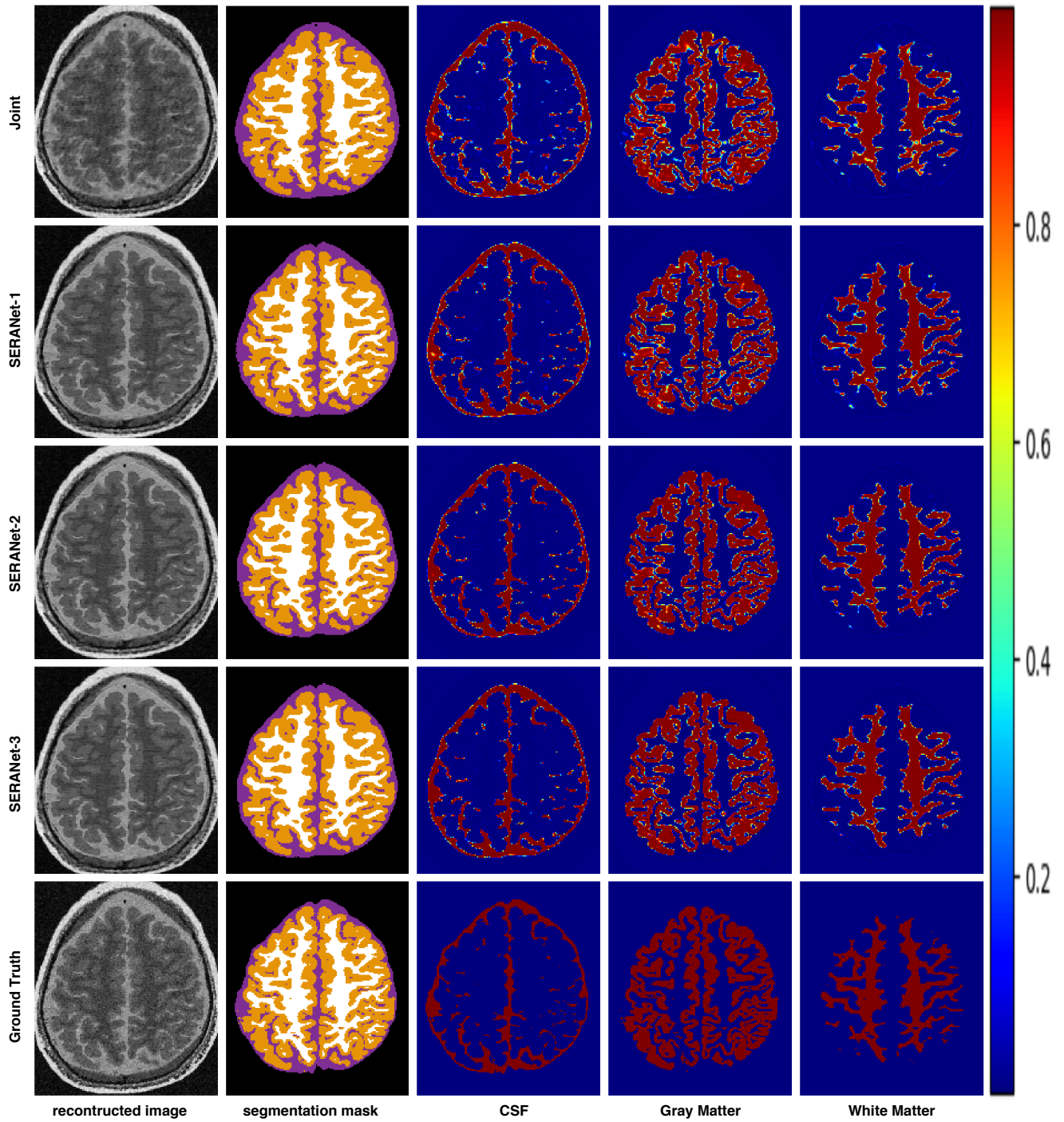


Figure 12. Intermediate attention maps of our recurrent attention model. It shows attention maps are gradually refined through increasing number of recurrence.